Active Short Circuit Tolerant Design of Permanent Magnet Assisted Synchronous Reluctance Machines

Gianvito Gallicchio, *Member, IEEE,* Mauro Di Nardo, *Member, IEEE,* Tianjie Zou, *Member, IEEE,* Krzysztof Paciura, Chris Gerada, *Senior Member, IEEE* and Francesco Cupertino, *Senior Member, IEEE.*

Abstract—The functional safety standard fulfillment could necessitate the active short circuit manoeuvre regardless the pre-operating condition of the electrical machine used in traction applications. This poses an additional and computationally-challenging requirement to the machine design as the permanent magnet (PM) demagnetization risk needs to be evaluated in the worst condition during the short circuit transient. This manuscript proposes a comprehensive design procedure of a PM assisted synchronous reluctance machine able to evaluate the full performance in the torque-speed plane including the short circuit current transient and the worst PM demagnetization condition in a time-efficient way. The computational efficiency is achieved evaluating the flux-current maps with a non-linear magnetic equivalent circuit carefully balancing the compromise between a faithful representation of the machine flux paths and computational effort. The methodology is adopted to perform a parametric design study varying two independent design variables and the number of poles considering the space and performance requirements of a heavy duty electric vehicle application. The compromise between overload capability and PM demagnetization during the short circuit is investigated defining the rationals of the final machine selection. One machine candidate is refined, manufactured and tested and the experimental results support both design procedure and design insights.

Index Terms—Analytical design, active short circuit, demagnetization, electric vehicle, finite element analysis, functional safety, magnetic equivalent circuit, permanent magnet, safe turn-off, synchronous reluctance

I. Introduction

HIGH power density, efficiency, reliability and relatively low cost are the typical design requirements of powertrains for electric vehicles [1]. Along with these design objectives, another critical factor when designing an electric drive system for an automotive application is the compliance with the functional safety standard ISO26262 [2]. Functional safety implies the absence of unacceptable risk due to hazards caused by malfunction in the electric and electronics systems [3]. Along with many others aspects, the standard addresses the faults detection and their mitigation and the transition of the electric drive system into a safe state. The powertrain is in a safe state when is not able to generate any torque, i.e. no current is flowing within the electrical machine [4]. This is usually realized by opening the main relay between the inverter and the battery regardless the operating condition of

G. Gallicchio, M. Di Nardo and F. Cupertino are with the Department of Electrical Engineering and Information Technology, Politecnico di Bari, Bari, 70126 Italy.

T. Zou and C. Gerada are with the Power Electronics, Machine and Control Group, University of Nottingham, Nottingham, NG7 2GT, UK.

K. Paciura is with Accelera by Cummins, Peterborough, PE15WS, UK.

the powertrain. Transitioning to a safe state could be required either as a reaction from a fault (e.g. battery overheating, critical sensor fault, etc.) which needs to be executed within a specified time or a request from the vehicle control unit (e.g. crash signal) [5]. There are mainly two approaches leading the electrical drive into a safe state: the active open and short circuit operations [6]. In the first case, the inverter switches are turned off so the electrical machines behaves as an uncontrolled generator; this operation is also referred as freewheeling (FW) as the current continues to flow via the freewheeling diodes. The second approach consists in actively short circuiting (ASC) the windings of the electrical machines using the inverter; in other words, all the lower switches are turned on while the upper are off or vice-versa. Adopting the first approach, the electrical machine experiences a lower post-fault currents and torque compared to the active short circuit method but could generate a high over-voltage on the dc-link potentially leading to disruptive values (for both capacitor and switches) if the pre-fault operating condition is in the high speed flux weakening region. On the other hand, the ASC approach avoids over-charging of the dc-link capacitor but the excessively high transient currents poses two serious challenges: the very high thermal stress in the power modules and the permanent magnet demagnetization due to very high peak current [7]. It is clear that the transition to a safe state should ideally be carried out with the minimum stress on the several powertrain components. The freewheeling approach could require the oversize of the dc-link capacitor while the short circuit one could lead to over-dimensioning the permanent magnets and/or affecting the power module thermal management. Both options have definitely cost and size implications.

A. Literature review

A literature review on this topic reveals that this problem has been mainly faced from the control point of view, i.e. proposing control strategies for the transition to the safe state which avoids any of the constituent component exiting the safe operating limits [8]. A straightforward solution is to adopt the freewheeling method up to a certain speed (approximately the base speed) and the active short circuit one for the remaining higher operating speeds [9] once verified the safe evolution of voltage, currents and torque whatever the pre-operating condition. Another more complicated approach requires the implementation of dedicated modulation strategies [6] or combination of open and short circuit operations [10].

Obviously, if the transition to the safe state is not time critical, the so-called soft turn-off strategies can be adopted which use the controller of the inverter to slowly transition to either ASC or FW. Clearly such soft techniques requires the inverter controller to remain functional [6]. Few research contributions have addressed this topic from a design perspective. From a machine standpoint, some contributions [11], [12] focus on the uncontrolled generator operation and on the design considerations aimed at achieving a safe FW operation. Other papers [13] investigate the machine response to a symmetrical short circuit and the key design factors affecting both steady state and transient behaviour [14]. These contributions give some design guidelines in terms of selection of both saliency ratio and PM flux aimed either at reducing the short-circuit current and so the PM demagnetization risk [14] or achieving a safe FW operation [11]. However, they do not investigate the performance sacrifice that must be accepted during the design stage if a safe open or short-circuit operation is required regardless the pre-operating condition. In addition, the relationship between geometrical parameters (such as pole pair, split ratio, tooth width, rotor geometry, etc.) and ASC or FW performance are not investigated. Accounting for the PM state at the peak demagnetizing current during the short circuit is highly time consuming as it requires the knowledge of the current transient which could be either evaluated by a full FEA or solving the differential equation knowing the machine parameters [15]; the same applies to the evaluation of the current and voltage during the FW operation. Solving a set of differential equations is definitely more time-efficient but still requires the knowledge of the full flux-current relationship. The latter could be highly non-linear in case of anisotropic synchronous machines and its evaluation could still require a relevant Finite Element (FE) effort. The flux current maps are also needed if the design procedure needs to consider performance indexes evaluated in different operating points, e.g. rated, overload or flux weakening, as usually requested by traction applications.

An alternative to the computational expensive FE modeling consists in adopting a non-linear magnetic equivalent circuits (MECs). On one hand, simplified non-linear lumped-parameters [16], [17] MECs have the clear advantage of the fast resolution but they can lack accuracy when analyzing high-saturated machines since such methods cannot properly capture the minor flux paths (e.g. slot opening, tooth shoe); thus a FE correction is generally required [18]. On the other hand, general distributed MECs [19], [20] can properly model all the machine flux paths at the cost of higher computational burden. The main modeling challenge is to find a good compromise between a faithful representation of the machine flux paths and a moderate number of nodes of the magnetic equivalent circuit. Regardless the MEC type, literature contributions have been focused on the model for a single case study without investigating the adoption of such approach within design exercises or optimizations.

B. Research contribution and paper structure

This paper attempt to fill these gaps by proposing a comprehensive design procedure of a permanent magnet assisted synchronous reluctance machine (PMaSyR) able to evaluate the full performance in the torque-speed plane including the short circuit current transient and the worst PM demagnetization condition in a very time-efficient way. The computational efficiency is achieved evaluating the full flux-current maps with a non-linear magnetic equivalent circuit (MEC) which carefully balance the compromise between a faithful representation of the machine flux paths (accuracy) and the MEC complexity (its number of nodes, i.e. computational effort).

This paper is structured as follow. First, it proposes a non-linear lumped-parameters MEC for PMaSyRM and validate its performance with finite element analysis (FEA) (Section II and III). The performance estimation method is then embedded within an analytical design procedure which drastically reduces the number of independent design variables (Section IV). The outlined design methodology is then used to perform a parametric design study varying the two independent design variables and the number of poles considering the space and performance requirements of a heavy duty electric vehicle application (Section V) focusing on the compromise between overload capability and PM demagnetization during the ASC. One machine candidate is then refined, manufactured and tested and the results are reported in Section VI.

II. MAGNETIC EQUIVALENT CIRCUIT

It is well-known that the torque produced by PMaSyRM (whose example geometry is shown in Fig. 1) can be expressed as:

$$T = \frac{3}{2}p(\lambda_d(i_d, i_q)i_q - \lambda_q(i_d, i_q)i_d) \tag{1}$$

where p is the pole pairs number, i_d and i_q are d- and q-axis currents, whereas λ_d and λ_q are the d- and q-axis flux linkages. The latter are non-linear function of both currents due to saturation and cross-saturation phenomena. It follows that, for a given machine geometry, the accurate computation of the flux and torque maps over the dq current plane require an accurate modeling the machine flux paths regardless the
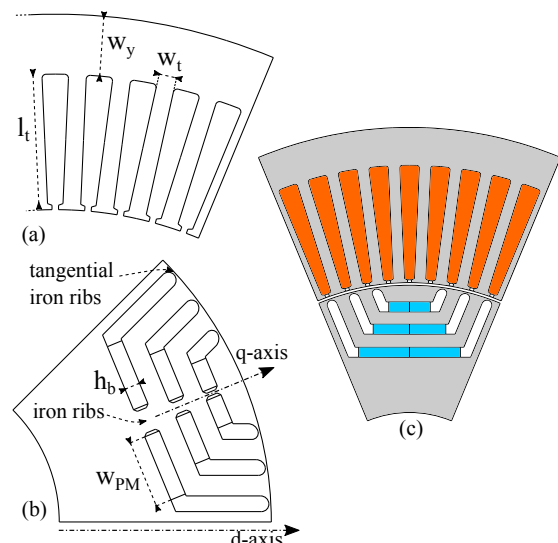
Fig. 1: (a) Stator (b) and rotor parametrization; (c) cross section of the machine.
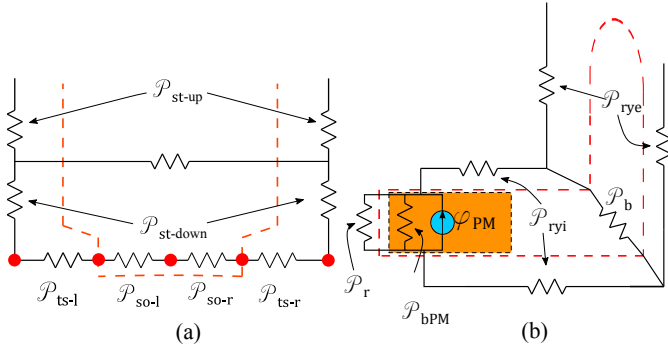
Fig. 2: (a) Slot and (b) flux barrier MEC representations.
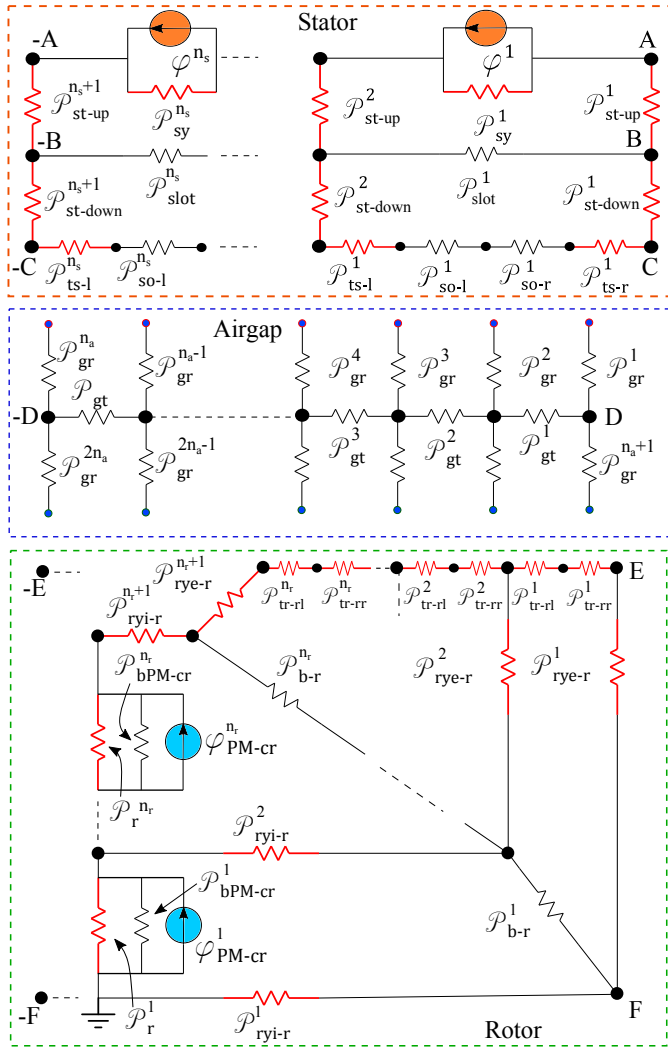
Fig. 3: Magnetic equivalent circuit.

operating conditions. This can be achieved adopting a unique magnetic equivalent circuit able to represent the main flux paths whatever the current supply condition. If a single stator slot and a single flux barrier is modeled as reported in Fig. 2, the whole adopted MEC can be generalized as shown in Fig. 3. The latter is able to fulfill the above mentioned requirement consisting of several linear and non-linear permeances representing the several linear and non-linear flux conducts and flux

generators representing the stator magneto motive force and the PM in the rotor. The next subsections detail the circuital modeling of the stator, rotor and airgap regions respectively, while subsection II-D outlines the procedure to non-linearly solve the MEC.

A. Stator modeling

The stator can be modeled by teeth, yokes, tooth shoe, slot and slot opening permeances. A permeance P_{sy} in parallel with a flux generator φ is adopted for modeling both the yokes flux path and the magnetomotive force due to the stator current, whereas each tooth is modeled by two permeances P_{st-up} and $P_{st-down}$. Finally, the permeances P_{so} and P_{ts} (left and right) model the slot opening and the tooth shoe of each slot, whereas P_{slot} models the slot (i.e. the slot leakage flux path). Each permeance contribution can be written as:

$$\mathscr{P}_x^i = \frac{\mu_0 \cdot \mu_x^i \cdot w_x^i}{l_x^i} l_{fe} \quad \text{for} \quad i = 1, ..., n_x \qquad (2)$$

where the subscript $_x$ can indicate either $_{sy}$, $_{st-up}$, $_{st-down}$, $_{ts-r}$, $_{ts-l}$, $_{slot}$, $_{so-r}$ or $_{so-l}$, while μ_x is the relative permeability of the respective stator part, w_x is the width of area crossed by the flux path and l_x is length of the same path and n_x is the number of permeance which models the considered stator part (i.e. the number of stator slots per pole n_s for the stator yokes, tooth shoes and slot opening, and $(n_s + 1)$ for the stator teeth). The expression of the flux generators φ_i can be derived considering the magnetomotive force (mmf) equation:

$$\mathbf{F} = z_Q \mathbf{M} \mathbf{I} \qquad (3)$$

where $\mathbf{F} = \begin{bmatrix} F^1 & F^2 & ... & F^{n_s} \end{bmatrix}'$, $I = \begin{bmatrix} i_a & i_b & i_c \end{bmatrix}'$ are the mmf and phase current vector, $\mathbf{M}$ is a $[n_s \times 3]$ matrix representing the position of the phase coils, n_s is the number of slots per pole and z_Q is the slot conductors number. Then, since each yoke can be represented by the above calculated F_i in series with a permeance $\mathscr{P}_{sy}^i$, by applying the Norton's theorem, the flux generators (φ^i) shown in Fig. 3 are computed as in (4):

$$\varphi^i = F^i \cdot \mathscr{P}_{sy}^i \qquad (4)$$

B. Rotor modeling

The rotor part of the MEC should be able to model all the main flux paths in order to accurately take into account the cross-saturation effect. In particular, each tangential iron bridge is modeled by two permeances ($\mathscr{P}_{tr-l}$ and $\mathscr{P}_{tr-r}$), whereas the radial ones by only one permeance $\mathscr{P}_r^i$ (one for each layer). The rotor flux guides are split in two parts: external and internal (denoted by the subscript $_{rye}$ and $_{ryi}$) and into right and left parts with respect to the q-axis (denoted by the subscript $_l$ and $_r$). Differently, the flux barrier (including the PM part) is modeled by linear permeance $\mathscr{P}_{b-PM}$ in parallel to a flux generator φ_{PM}. The mathematical expression of all these permeances can be written as:

$$\mathscr{P}_y^i = \frac{\mu_0 \cdot \mu_y^i \cdot w_y^i}{l_y^i} l_{fe} \quad \text{for} \quad i = 1, 2, ..., n_y \qquad (5)$$

where the subscript y can indicate either the iron bridges, flux guides or flux barriers, whereas n_y is the number of permeances which models the considered rotor parts (i.e the number of flux barriers n_r for the iron ribs and flux barriers or $n_r + 1$ for the rotor flux guides).

C. Airgap modeling

The airgap region has been modeled by a combination of radial and tangential permeances with the aim of accurately capture the airgap flux density. Once the level of discretization n_a is defined, the airgap network is characterized by n_a radial permeances facing the stator, n_a radial permeances facing the rotor and $n_a - 1$ tangential permeances. The radial components can be modeled as follows:

$$\mathscr{P}_{gr}^i = \frac{\mu_0 \cdot \Delta\alpha \cdot r_r}{g_{eq}} \cdot l_{fe} \qquad \text{for} \quad i = 1, 2, ..., 2n_a \quad (6)$$

where r_r is the airgap radius, g_{eq} is the equivalent airgap thickness, $\Delta\alpha$ is the airgap discretization which depends on the number of considered airgap permeances n_a:

$$\Delta\alpha = \frac{\pi}{2p \cdot n_a} \qquad (7)$$

When considering the stator side permeances, g_{eq} is equal to half the mechanical airgap g if the considered permeance faces the stator tooth or the stator tooth shoe, whereas it is equal to $\frac{g}{2} + \frac{l_{so}}{2}$ if it faces the stator slot opening, where l_{so} is the slot opening height. Differently, g_{eq} is always equal to half the mechanical airgap one g when considering the rotor side permeances. The tangential components can be calculated as:

$$\mathscr{P}_{gt}^i = \frac{\mu_0 \cdot g}{\Delta\alpha \cdot r_r} \cdot l_{fe} \qquad \text{for} \quad i = 1, 2, ..., n_a - 1 \quad (8)$$

The selection of n_a is the result of the trade-off between accuracy and computational burden.

D. MEC resolution

For a given machine geometry and supply condition (in terms of i_d and i_q), the above described MEC, consisting of n_N nodes can be solved using the nodal-voltage method, whose formulation can be written as follows:

$$\mathscr{P} \cdot \mathbf{V} = \mathbf{\Phi} \qquad (9)$$

In (9) $\mathscr{P}$ is the $[n_N \text{ x } n_N]$ matrix containing the nodal permeances (whose diagonal terms are the sum of the permeances connected to the ith node, while the negative sum of the permeances between the nodes i^{th} and j^{th} constitute the off-diagonal terms), $\mathbf{V}$ represents the nodal-voltage vector whereas $\mathbf{\Phi}$ is the vector of the flux generators. The permeance matrix $\mathscr{P}$ can be assembled as in eq. (10) [21]:

$$\mathscr{P} = \mathbf{L^T}(\mathscr{P}_{lin} + \mathscr{P}_{fe} \cdot \mu_{\mathbf{fe}})\mathbf{L} \qquad (10)$$

where $\mathscr{P}_{lin}$ and $\mathscr{P}_{fe}$ are diagonal $[n_B \text{ x } n_B]$ matrices (being n_B the number of branches) which account for the branch permeances of linear and non-linear parts of the machine respectively without considering the relative permeability. The diagonal matrix $\mu_{\mathbf{fe}}$ represents the relative permeability of the non-linear parts and has to identified iteratively. The term L is

TABLE I: Machine parameters

Parameter	Value	Units
Outer stator radius	144	mm
Stack length	155	mm
Pole pair	8	/
Cooling capability	40000	W/m^2
Airgap thickness	1	mm
Stator Lamination material	JNEX900	//
Rotor Lamination material	35HXT780T	//
Base speed	5000	rpm
Maximum speed	15000	rpm

the $[n_B \text{ x } n_N]$ incidence matrix and represents the connections between branches and nodes and its elements could be equal to 0 if the two nodes and branch are not connected or ± 1 otherwise (the sign is positive or negative according to the supposed flux direction). The adopted iterative method is the Newton-Raphson one:

$$\epsilon = \mathscr{P} \cdot \mathbf{V} - \mathbf{\Phi} \qquad (11)$$

where ϵ is the residual whose reduction is the goal of the iterative procedure. Using the residual, $\mu_{\mathbf{fe}}$ is updated at $k+1$ step by calculating $\mathbf{V}$ at the same step:

$$\mathbf{V}(k+1) = \mathbf{V}(k) - \mathbf{J}(k)^{-1}\epsilon(k) \qquad (12)$$

where $\mathbf{J}(k)$ is the Jacobian matrix at the step k, calculated as:

$$\mathbf{J} = \mathscr{P} + \mathbf{L^T}(\mathscr{P}_{fe} \cdot \mathbf{A} \cdot \dot{\mu}_{\mathbf{fe}})((\mathbf{LV_d U}) \cdot \mathbf{L}) \qquad (13)$$

where $\mathbf{A}$ is the flux-crossed area of the non-linear elements, $\dot{\mu}_{fe}$ is a diagonal matrix ($[n_B \text{ x } n_B]$) whose elements are the derivative of $\mu_{\mathbf{fe}}$ with respect to the magnetic field intensity H. $\mathbf{V_d}$ is the diagonal matrix of the nodal voltages $\mathbf{V}$, while $\mathbf{U}$ is a ($[n_N \text{ x } n_N]$) matrix which represents the connections between each node (i.e. if the ith and j^{th} nodes are connected is 1, otherwise is 0). The MEC solving procedure is made of the following steps.

1) Definition of the machine geometry, thus leading to the determination of $\mathscr{P}_{lin}$ and $\mathscr{P}_{fe}$.
2) Definition of the supply condition in terms of i_d and i_q
3) Initial guess of $\mu_{\mathbf{fe}}$
4) Calculation of the $\mathscr{P}$ using (10) and calculation of the residual ϵ.
5) Calculation of the Jacobian matrix J using (13) so to obtain the new nodal voltages solution and update $\mu_{\mathbf{fe}}$.
6) Step 4 and 5 are re-called until ϵ lies within a predefined threshold.

III. PERFORMANCE ESTIMATION AND FE VALIDATION

Once the MEC is solved, so the flux flowing in each branch of the circuit is known as its associated flux density, it is possible to calculate the global quantities such as flux linkages, torque and stator iron losses, which are all needed for design purpose.

The overall d- and q-axis flux linkage can be directly calculated from the flux flowing within the stator yokes φ_y. In

particular, the abc fluxes can be calculated knowing the matrix $\mathbf{M}$ as in (14):

$$\boldsymbol{\lambda_{abc}} = 2 \cdot p \cdot z_Q \cdot \boldsymbol{\varphi_y} \mathbf{M} \tag{14}$$

where the term $2 \cdot p$ is required only if one pole of the machine is analyzed. Then, the d- and q-axis flux linkage $\lambda_d(i_d, i_q)$ and $\lambda_q(i_d, i_q)$ are determined using the Park transformation.

Knowing the flux density values within each stator yoke and tooth parts, the respective maximum values for each component (yoke B_y and tooth B_t), can be calculated and used within the Steinmetz equation to obtain a good estimation of the stator iron losses:

$$\begin{aligned} P_{fe-st} = k_{fe}\{M_y[k_h f^\alpha B_y^\beta + k_e(fB_y)^2 + \\ + M_t[k_h f^\alpha B_t^\beta + k_e(fB_t)^2]\} \end{aligned} \tag{15}$$

where k_{fe} is a correction factor, M_y and M_t are the yoke and teeth masses, whereas k_h, k_e, α and β are coefficients that depend on the lamination material.

The above described performance estimation method based on the non-linear MEC has been applied to the machine whose main data are shown in Table I and whose geometry is shown in Fig. 1c. In the next three sub-sections, the MEC is FE-validated first comparing both local and global variables in different operating conditions for a specific design and then different slots/barriers combinations are considered to assess the MEC generality. The last sub-section reports a sensitivity analysis investigating the role of the airgap discretization of the results accuracy.

A. In-depth FE validation

Fig. 4a, b and c reports the radial airgap flux density as function of the spatial angle for three different supply conditions, no-load, only i_d and only i_q compared to the respective FE counterparts. A good agreement between analytical and FE calculations is visible also in the challenging supply condition of $i_d = 0$, i.e. when the armature flux is opposed to the PM one. The second row of the same figure, i.e. Fig. 4d, e and f, report the comparison between analytical and FE computations of the d- and q-axis flux linkages and the torque in the dq current plane. Also in this case, an excellent match is obtained for the entire set of considered operating conditions. The last row of Fig. 4 shows the flux densities within a stator tooth, yoke and the stator iron losses as function of the d- and q-axis current.

B. FE validation for different slots/barriers combinations

With the aim of further validating the proposed approach, the latter has been applied also considering different slots/barriers combination. The results of this exercise are reported in Fig.5, whose first row reports the cross section of the considered machines. The second row highlights the excellent agreement in the airgap flux density estimation, even when considering a high number of slots. The excellent match in terms of the torque in the d-q current plane is finally shown in the third row of the same figure.

The comparison with the respective FE variables reveals the capability of the proposed MEC to accurately estimate the
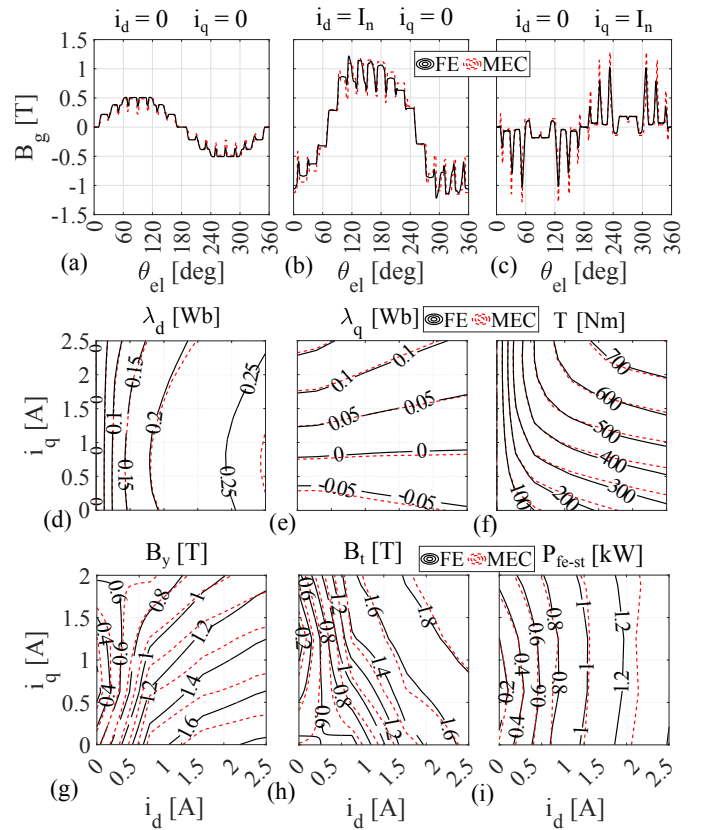
Fig. 4: Comparison between analytical and FE computations of the airgap flux density in different operating conditions (a,b,c), d-axis flux (d), q-axis flux (e) torque (f), flux densities within yoke (g) and tooth (h), and stator iron losses maps.

machine performance in the entire dq current plane with a negligible computational time. Indeed, the latter is between 6 and 12 seconds (depending on the number of pole pairs, number of slots and barriers) for mapping a static 10x10 grid in the dq plane using a medium performance workstation, while the FE computational time is around 500 seconds.

C. Airgap discretization sensitivity analysis

The above results have been obtained considering a fixed discretization of the airgap region. Fig. 6 reports the results of a sensitivity analysis assessing the estimation error of the first harmonic of the airgap flux density at rated MTPA condition as function of the number of airgap discretization n_a for three different slots/barriers combinations. The same figure also reports the computational time required to map the entire d-q current plane with a 10x10 grid. These analysis show that it is not necessary to increase n_a above 40 for all the three cases. Clearly, this value is dependent by the number of pole pairs, slots per pole per phase, number of barriers and other geometrical parameters.

IV. DESIGN PROCEDURE

The above described performance evaluation method perfectly suit to be embedded within a systematic design procedure given its computationally efficiency. The adopted design methodology starts with the definition of two independent
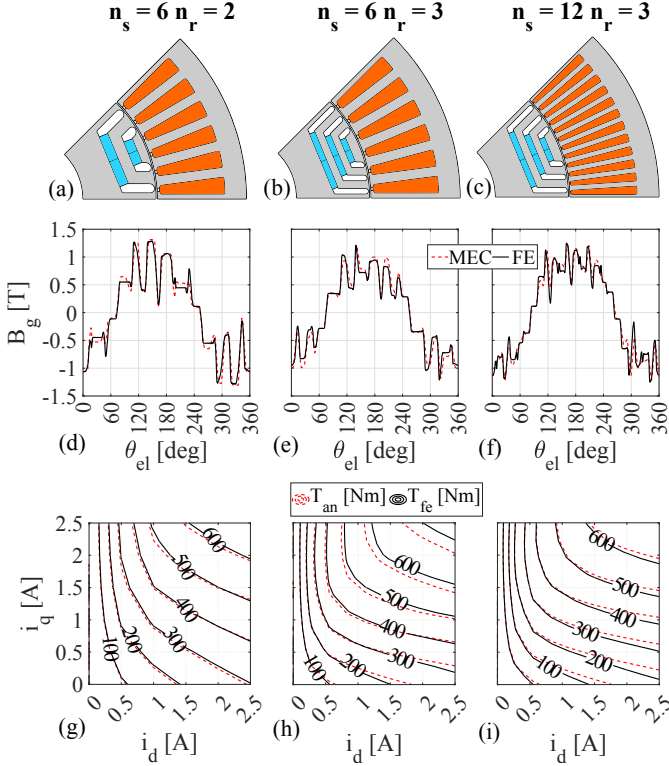
Fig. 5: Cross section of the machine under investigation (a,b,c), airgap flux density at rated condition at MTPA (d,e,f), torque maps in the d-q current plane (g,h,i).
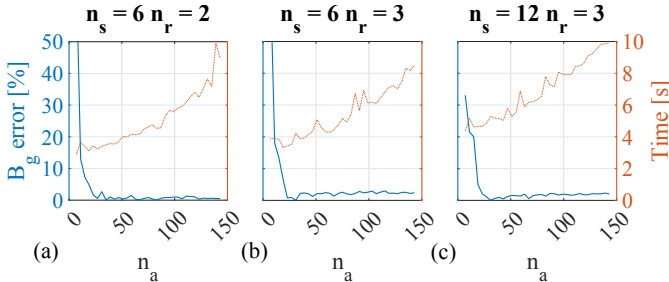
Fig. 6: Error between MEC and FE computations of the first harmonic of B_g and computational time as function of the n_a.

design variables, namely split ratio sr and iron ratio ir, similarly to idea proposed in [22]–[24] for both low and high speed synchronous reluctance machines. The first independent design variable is the ratio between the airgap r_r and the stator outer radius r_s, while the second one is the ratio between the stator tooth width w_t and the linear slot pitch τ_s:

$$sr = \frac{r_r}{r_s}, \quad ir = \frac{w_t}{\tau_s} \tag{16}$$

The definition of these two variables allows the calculation of the remaining geometrical parameters via physical and geometrical considerations for a give outer envelope (i.e. stator outer radius r_s and stack length l_{fe}). Once the complete stator and rotor geometry is expressed as a function of sr and ir, it is possible to use the developed MEC to estimate the full performance of each machine design in the design plane $sr - ir$.

The tooth width w_t obviously follows from the definition of the iron ratio ir:

$$w_t = \tau_s \cdot ir = \frac{2\pi \cdot sr \cdot r_s \cdot ir}{6qp}. \tag{17}$$

The yoke thickness can be derived by imposing a proportionality between the yoke and the tooth flux densities

$$B_y = k_t \cdot B_t \tag{18}$$

where k_t is less than one if the tooth is designed to be sligtly more magnetically loaded than the yoke. Indeed, the tooth flux density B_t can be calculated from the following equation:

$$B_t = B_g \cdot \frac{\tau_s}{w_t} \tag{19}$$

where B_g is the first harmonic airgap flux density while the yoke width w_y can be derived as:

$$w_y = \frac{B_g}{B_y} \frac{r_r}{p} \tag{20}$$

Substituting (18) and (19) into (20) is possible to obtain the relationship between tooth and yoke width:

$$w_y = \frac{r_r \cdot w_t}{p \cdot k_t \cdot \tau_s} = \frac{r_s \cdot sr \cdot ir}{p \cdot k_t} \tag{21}$$

Since the r_s is fixed, the tooth length follows by geometrical considerations for each $sr - ir$ combinations, whereas a slot opening of 0.25 p.u. (of the slot pitch) and the tooth shoe height of 0.3 (in p.u. of the tooth width) are imposed for all the designs.

The rotor geometry (see Fig. 1) can be described by several parameters, which include the number of flux barriers n_b, their angular position along the airgap periphery, their thickness along the q-axis and the amount of PM volume, expressed in terms of PM width. By imposing an uniform distribution of the equivalent rotor slots and the same permeance for each barrier, it is possible to uniquely determine their angular position at the airgap and their radial thickness once n_b is chosen [22]. Then, the width of the structural iron bridges is calculated considering a simplified formulation [25] which only accounts for the steady-state centrifugal force.

The selection of PM amount, which represents another design degree of freedom, can be identified imposing the natural compensation condition, which leads to the widest constant power speed range for a given current module (usually the rated one I_n) [26]:

$$\lambda_q(0, I_n) = \lambda_{q-PM}(0, I_n) + \lambda_{q-rel}(0, I_n) = 0 \tag{22}$$

where λ_{q-PM} and λ_{q-rel} are the PM and reluctance flux linkages which are non-linear function of the current.

The rated current can be identified constraining several performance indexes such as surface or linear current density or the joule losses. In this study, it has been chosen to constrain the overall stator losses encompassing both joule and iron losses. In other words, the rated current is calculated with the following equation (23):

$$I_n = \frac{1}{3N_s} \sqrt{\frac{k_{fill}A_{slots}}{2\rho_{cu}(l_{fe} + l_{ew})}(2\pi r_s l_{fe}k_{cool} - P_{fe-st})} \tag{23}$$

where N_s is the turns' number in series per phase, k_{fill} is the slot filling factor, A_{slots} is the slots area, ρ_{cu} is the copper resistivity, l_{ew} is the end-winding length whereas P_{fe-st} are the stator losses at rated conditions which can be calculated still using (15). The coefficient k_{cool} represents the cooling system capacity, i.e. the ratio between the maximum allowed losses and the external stator surface. This choice leads to a more fair comparison between different machine designs as all of them can approximately share the same cooling system [24]. The calculation of the rated current requires the knowledge of the iron losses, which in turn can be calculated only after the definition of both current and PM dimension; the latter can in turn be calculated once the current is known. Clearly, an iterative procedure is needed for the calculation of both rated current and PM dimension while keeping constant the overall stator losses. To do so, the following iterative procedure has been adopted for each machine candidate defined by the combination $sr - ir$.

1) To start the iteration procedure a first guess of B_y and B_t is supposed which allows the calculation of the iron losses via (15).
2) Then, the rated current is calculated using (23).
3) Using the above calculated current it is possible to solve the MEC for different values of the PM dimensions until the natural compensation condition reported in (22) is satisfied.
4) Then, once the PM dimensions are defined, the maximum torque per ampere condition at the rated current is iterativly searched via the MEC. Once found, the correct values of both iron flux densities B_y and B_t are obtained and the iron losses calculation can be updated.
5) If the error between the initial and updated values of the iron losses lies within a predefined threshold the algorithm ends; otherwise the rated current is re-calculated and the procedure restart from step 2.

V. COMPARATIVE DESIGN EXERCISE

This section first outlines the rationals behind the selection of the performance indexes considered in the comparative design (V-A), then presents the analysis for different pole pairs ($p = 2 - 6$) in the design plane $sr - ir$ (V-B). The trade-offs to consider during the selection of the best designs are then discussed in subsection V-C while the performance of the optimal solutions are introduced in subsection V-D. The last subsection assess the trade-off between overload and PM demagnetization during the worst ASC for designs featuring different poles and cooling system capability.

A. Selection of the performance indexes

The proposed design procedure and MEC-based performance estimation methodology can be used to assess the behaviour of several performance indexes. Indeed, it is possible to calculate the full performance in the entire torque-speed plane for each machine design and then evaluate how a certain performance index changes in the design plane $sr - ir$.

For example, Fig. 7a reports the contour of the overload torque at MTPA condition in the design plane $sr - ir$ for

a given pole pair ($p = 4$) when using the data outlined in Table I. This operating condition is particularly challenging to be estimated as it requires the capability to account both saturation and cross-saturation phenomena. The second and third subplots (Fig. 7b and c) show the rated torque evaluated at the base and maximum speeds respectively in the same design plane.

Stating the obvious, the calculation of the torque at the maximum speed for the rated current requires the knowledge of the control locus which can be only calculated if the full d-q flux-current maps are known. The FE evaluation of these indexes would be particularly computationally challenging; instead, adopting the proposed approach the time required to map the $sr - ir$ design plane with a 10x10 grid is about 20 minutes. Comparing the first two subplots (Fig. 7a and b), it is possible to observe that the design featuring the best overload torque is not exactly the one showing the best rated torque one and vice-versa. This is mainly due to the saturation effect, which obviously increases in overload, and leads to optimal torque-wise design to slightly higher ir, i.e. bigger iron dimension (both w_t and w_y) and split ratio sr. The contour of the rated torque at the maximum speed resembles the one evaluated at the base speed (Fig. 7b and c). This is a direct consequence of the selected PM design criteria; indeed, the natural compensation criterion imposes that the rated power at maximum speed is equal to the one at base
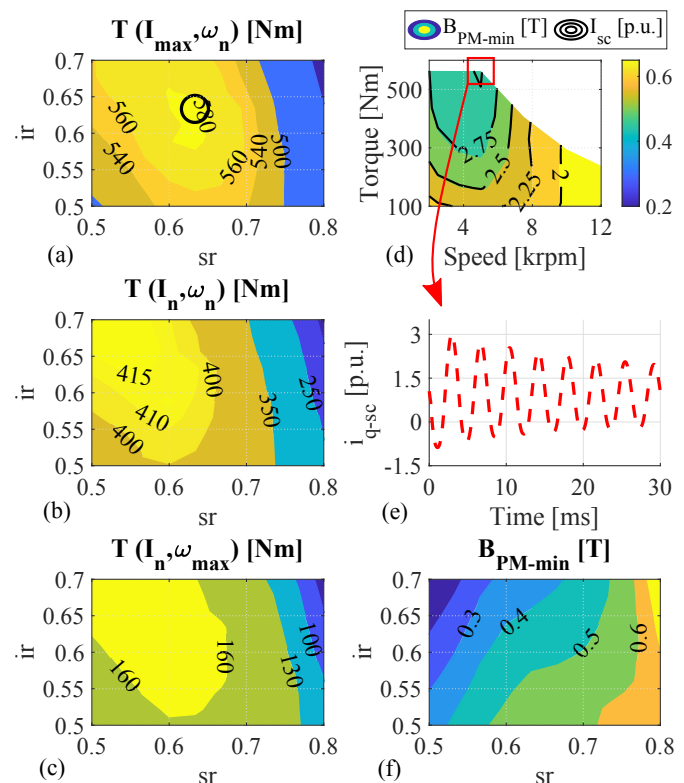
Fig. 7: (a) Overload torque contour at base speed, (b) rated torque contour at base speed, (c) rated torque contour at maximum speed in the $sr - ir$ plane (d) minimum PM flux density and maximum p.u. short circuit current in the torque-speed plane, (e) q-axis short-circuit transient current example, (f) minimum PM flux density contour in the $sr - ir$ plane.

speed, therefore the rated torque contour at the maximum speed is almost a scaled version of the base speed one.

For each machine candidate, the evolution of the 3-phase short-circuit current can be calculated for every pre-fault condition in the respective torque-speed plane. Indeed, knowing the full flux-current maps, it is possible to solve the set of differential equations governing the short circuit as reported in [15], [27]. Fig. 7d shows the maximum value of the q-axis transient short circuit current (i.e. the one aligned with the PMs I_{sc-wc}) in the torque-speed plane along with the minimum value of the PM flux density B_{PM-min} experienced in that unfavourable condition. Such analysis has been carried out for the design highlighted with the circle marker in Fig. 7a. These two contours (I_{sc-wc} and B_{PM-min}) have a very similar trend, implying that higher I_{sc-wc} leads to higher PM demagnetization risk, i.e. lower PM flux density. Fig. 7e reports the time-evolution of the q-axis current considering the pre-fault operating condition highlighted with the red square marker Fig. 7d; the worst demagnetizing current usually occurs within the first two/three electrical periods. The worst pre-fault operating condition in terms of I_{sc-wc} and so PM demagnetization risk is the overload one at the MTPA. This is a direct consequence of the proportionality between pre-fault flux module and maximum short circuit current along the PM axis as suggested in [15], [28]. Supposing that the worst pre-fault short circuit condition is always the overload MTPA regardless the machine design (i.e. independently of $sr-ir$), the short circuit demagnetization check can be performed systematically for the entire design plane $sr-ir$ as shown in Fig. 7f. The calculation of the worst short circuit current I_{sc-wc} and the B_{PM-min} calculation with the MEC requires an additional computational time of 6 seconds for each solution of the $sr-ir$ plane thus leading to a total computational time of 30 minutes for 100 designs (i.e. 18 seconds per machine candidate).

B. Overload and short circuit PM demagnetization analysis

The design procedure described in the previous section has been applied considering the following comparative workflow:

- for each pole pair scenario, a design plane $sr-ir$ is obtained as the ones shown in the first row of Fig. 7;
- for each machine of the above plane, the worst case short circuit current is calculated from the flux maps; the latter current value is used to solve the MEC and calculate the PM demagnetization state;
- the above information are used to select the optimal machine (torque wise) in the design plane $sr-ir$ for each pole pair scenario.

The first row of Fig. 8 reports the overload torque as a function of the design variables sr and ir for each considered pole pairs scenario. It is worth noticing that the maximum torque location (highlighted with a black circle) in the $sr-ir$ plane moves towards higher split ratio and lower iron ratio as poles increase. The reason behind such trend can be inferred considering the different losses distribution which changes with the number of poles. Indeed, the overall losses are kept constant regardless p (see eq. (23)), therefore higher number

of poles implies a higher iron losses quota with respect to the Joule one as clearly shown in the second row of Fig. 8 which reports the P_{fe} loci. It follows that the iron losses play a major role as p increases thus leading to different shape of the rated current contour (eq. (23)) also shown in same figures. Therefore, the maximum torque design moves towards the zone of the design plane featuring lower stator iron losses. The third row of Fig. 8 reports the maximum current against the PMs during a three phase short circuit I_{sc-wc} (in p.u. of the rated one) when considering a pre-fault operating condition equal to overload one at the MTPA. It can be noticed that I_{sc-wc} increases with the split ratio while it is barely influenced by the iron ratio, regardless the pole number. Also, for a given $sr-ir$ combination, the p.u. value of I_{sc-wc} tends to decrease with the number of poles. The same subplots also report the minimum value of the flux density in the PMs B_{PM-min} in the worst short circuit condition. The black dashed line defines the limit between the demagnetized and non-demagnetized designs that for the considered PM material and temperature is around 0.4 T. Despite the short-circuit current tends to worsen as sr increases, B_{PM-min} presents an opposite trend, i.e. it gets better with the split ratio. In addition, the minimum PM flux density also tends to decrease as ir increases, regardless the number of poles. This is due to the fact the minimum value of the PM flux density during the short circuit does not only depend on the short-circuit current but also on the machine geometry (i.e. split ratio, PM width and height and so on) which changes according to the $sr-ir$ combination. Differently, considering a given $sr-ir$ combination but different pole pairs, B_{PM-min} tends to decrease with p; consequentially, the portion of the design plane which demagnetize is bigger for low poles designs (see upper-left area defined by the dashed black line). The rationale behind the above trends can be analysed considering both the PM state before the short circuit $B_{PM-prefault}$ and the q-axis flux due to the current in the worst case short-circuit scenario $\lambda_{q-rel}(I_{sc-wc})$. The fourth row of Fig. 8 shows both these two quantities and the analysis of their trends leads to the following considerations.

- $B_{PM-prefault}$ tends to decrease for higher iron ratio. Indeed, higher iron ratio implies lower rotor flux barriers height which in turn determines smaller space for the PM placement. This leads to weaker PMs (i.e. with lower flux density values) which are more prone to demagnetize during the short circuit even with low p.u. values of maximum short circuit current.
- $\lambda_{q-rel}(I_{sc-wc})$ have an opposite behaviour respect with the short circuit current I_{sc-wc}, i.e. it is almost ir-independent and increases as sr decreases regardless the pole pairs although its variation within the design plane is more pronounced for lower poles. This behaviour can be mainly ascribed to how the q-axis inductance in short circuit condition change in the design plane.
- The portion of the design plane $sr-ir$ suffering the PM demagnetization during the short circuit corresponds to area where the pre-fault PM flux density is low and the q-axis reluctance short circuit flux is high, i.e. the upper-
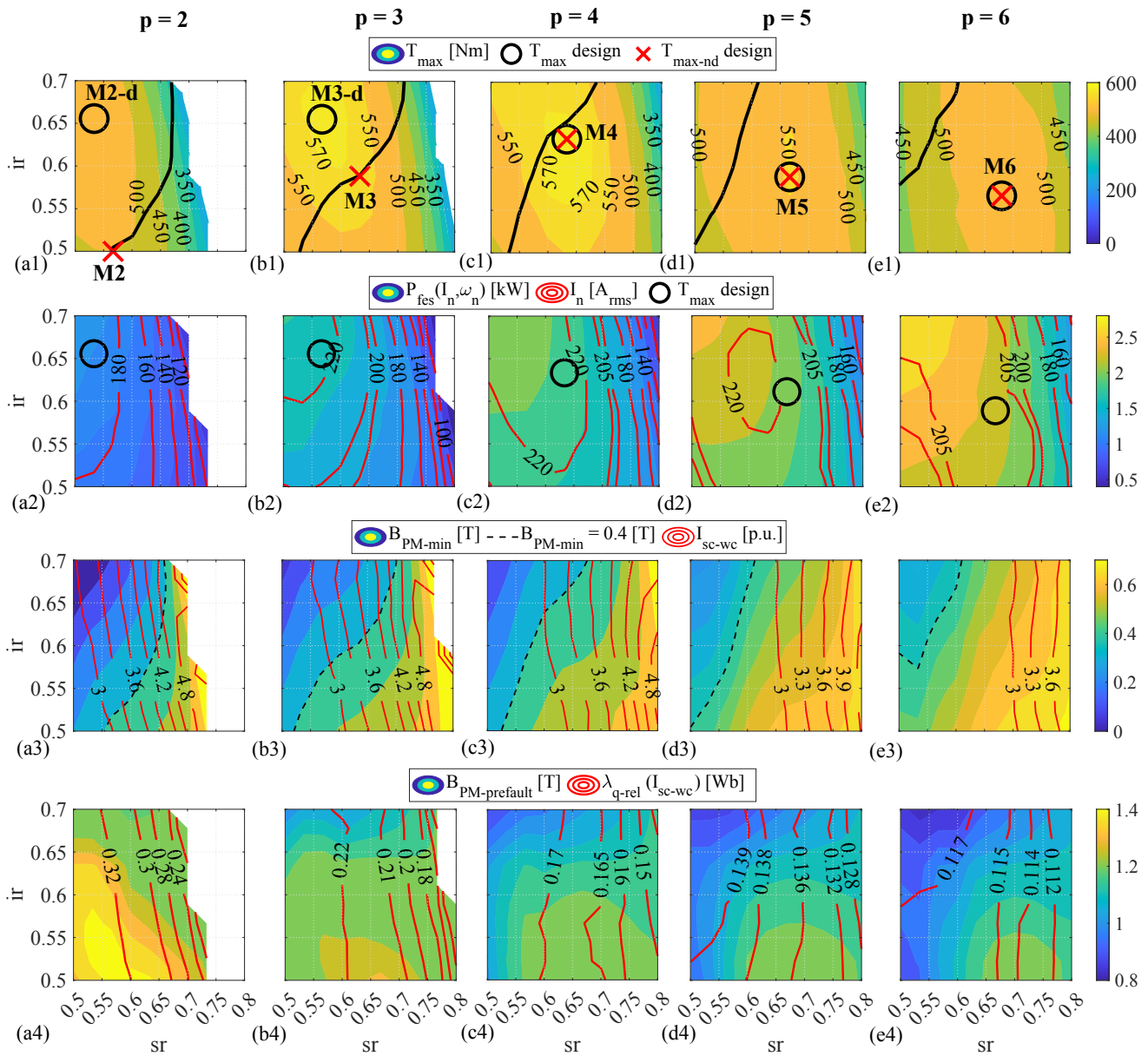
Fig. 8: (1) Average torque contour loci, (2) iron losses P_{fe-st} and rated current I_n contour loci, (3) maximum short circuit current I_{sc-ws} in p.u. of the rated one and minimum value of flux density in the PMs contour loci, in the design plane split/iron ratio $sr - mr$ and for different pole pairs scenario (a,b,c,d,e).

left zone of the design plane.

- The design region of the $sr - ir$ plane suffering the PM demagnetization during the short circuit shrinks as the pole pairs increases mainly because the q-axis reluctance short circuit flux decreases with p. Indeed, both $B_{PM-prefault}$ and $\lambda_{q-rel}(I_{sc-wc})$ decreases as p increases when considering the same $sr - ir$ combination. However, the latter decreases much more than the former; for example comparing $p = 2$ and $p = 6$ with $sr = 0.55, ir = 0.65$, the $B_{PM-prefault}$ decreases of about 25% while the reluctance short circuit flux $\lambda_{q-rel}(I_{sc-wc})$ decreases of about 65% when going from low to high pole pairs.
- As a direct consequence, comparing the contours of B_{PM-min} and $B_{PM-prefault}$, these are very different

at low pole pairs while becomes much more similar for high p because of both the reduction of $\lambda_{q-rel}(I_{sc-wc})$ and its reduced variation within the design plane.

C. Machine selection: overload and ASC survival trade-off

The selection of the optimal machine, i.e. the region of the design space $sr - ir - p$ of major interest where to focus the design refinement effort, has to take into account many performance indicators. Among the many, the most impactful are the overload capability and eventually the constraint imposed by the PM demagnetization during a three phase short circuit (if this is a design requirement).

The demagnetization limits highlighted with the dashed black lines B_{PM-min} contours of Fig. 8 are also reported

in the overload torque loci always shown in the first row of the same figure.

If the constraint of the PM demagnetization during the short circuit has to be taken into account, the location of the optimal torque-wise design in the $sr - ir$ plane changes (see the red crosses). In particular, the best torque designs with and without considering this constraint are completely different for low pole pairs and their difference decreases as p increases till they coincide for higher poles. This is clearly due to the fact that a) the unconstrained maximum torque design moves towards higher split ratio and lower magnetic ratio as p increases and b) the design area suffering the PM demagnetization issue shrinks with the number of poles. It can be concluded that the PM demagnetization constraint during the worst short circuit condition affects the machine selection mainly when considering low pole designs.

D. Analysis of the optimal machines

This sub-section reports the analysis of the optimal torque-wise designs selected from each design plane. In particular, for the low-poles scenarios (i.e. 4 poles and 6 poles) two optimal machines can be identified, namely M2-d and M2 and M3-d and M3, since the location of the optimal solution changes whether the constraint on the PM demagnetization is taken into account or not. Differently, higher pole pairs imply that the location of the best solution does not depend on the demagnetization constraint (i.e. the excluded portion of the design plane does not contain the optimal torque solution). This consideration is highlighted in Fig. 9 which reports the optimal design variables as function of the pole pairs with and without considering the constraint on the PM demagnetization (see the subscript nd in the figure legend). The geometries of these design are shown in the second row of Fig. 10 along with the flux density distribution (calculated using FEA) during the worst short-circuit condition.

The first row of same figure shows the rated power and the overload torque as a function of the speed of the optimal designs with and without considering the demagnetization constraint.

Analysing this figure it is possible to draw the following considerations.

- All the machines meet the natural compensation criterion thus indirectly validating the PM dimension calculation procedure.
- Both overload torque and rated power first increase and then decrease with the pole number, regardless if the selection of the optimal machine takes into account the PM demagnetization (e.g. M2-d or M2).
- The FE computation of the flux density within the PMs confirms the results of the analytical approach. Indeed, the analytical non-demagnetized machine during the short circuit presents a minimum value of the B_{PM} higher than the knee value, whereas the analytical demagnetized ones (i.e. M2-d and M3-d) presents a lower value of $B_{PM-knee}$.

It follows that the designs M2, M3, M4, M5 and M6 can survive an ASC manoeuvre whatever the pre-operating
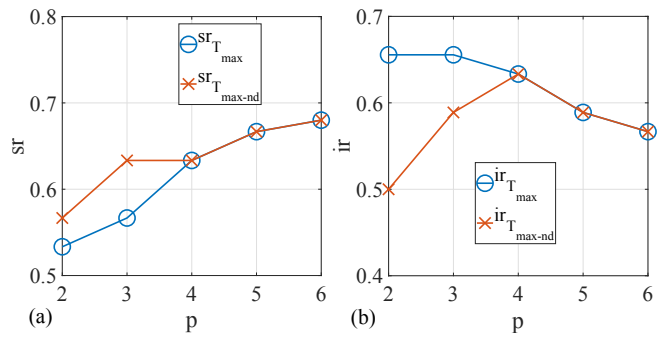
Fig. 9: sr (a) and ir (b) of the optimal designs for different pole pairs.
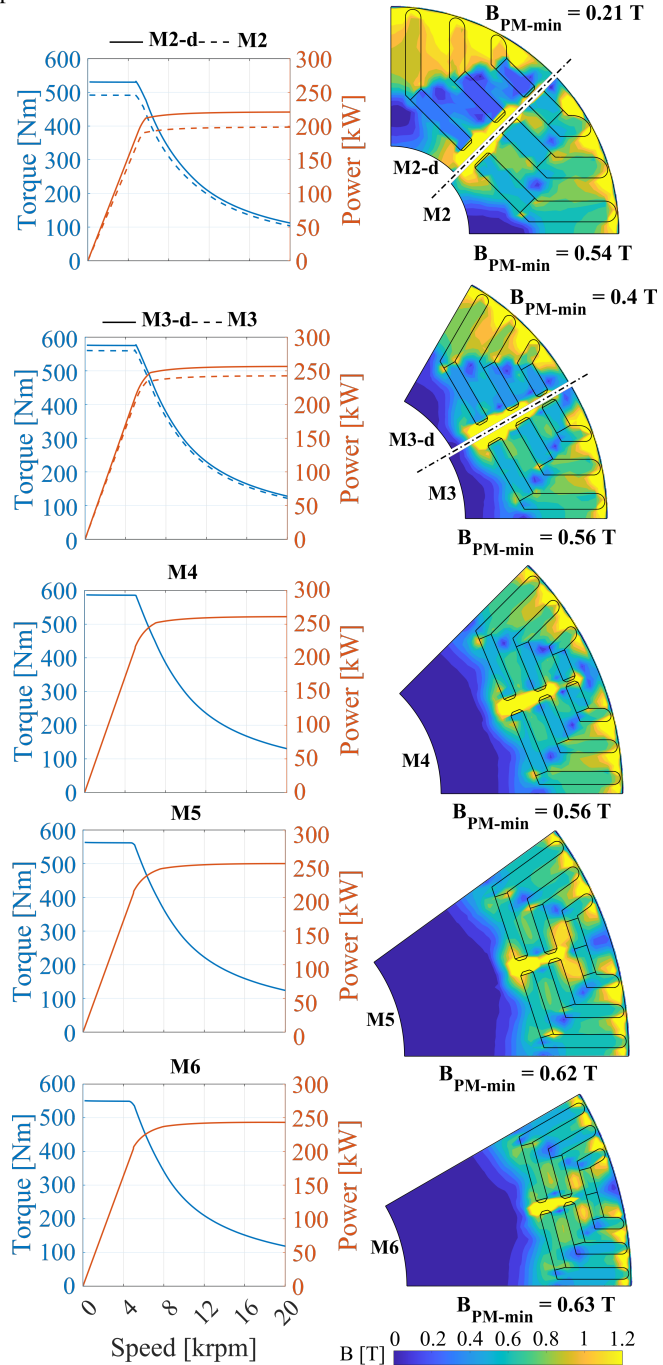
Fig. 10: Performance, rotor cross section and flux density in the PMs during ASC of the maximum torque designs.
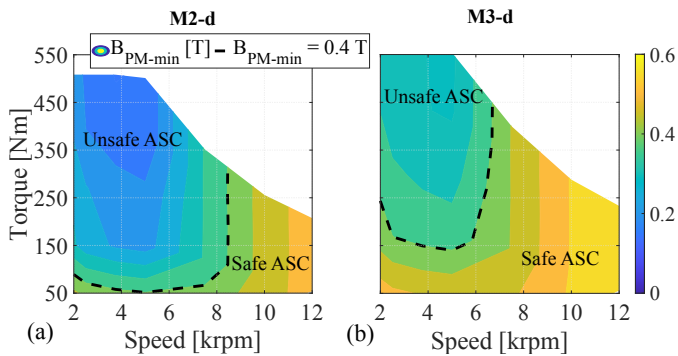
Fig. 11: M2-d (a) and M3-d (b) safe and unsafe regions in the torque-speed plane.

condition in the torque-speed plane; indeed, their PMs would not suffer any demagnetization issue. On the contrary, the solutions M2-d and M3-d can be still considered acceptable designs, but the ASC operation is safe only in a limited area of the torque-speed plane as shown in Fig. 11. The latter reports the minimum value of the PM flux density during the short-circuit in the torque-speed plane (i.e. as function of the pre-fault condition). The safe region is particularly limited when considering the 4-poles machine; indeed, in such case the ASC can be applied only if the machine is operating in a part of the flux weakening region.

E. Sensitivity analysis for different k_{cool}

The analysis reported up to this point have been performed considering a certain cooling system capability ($k_{cool} = 40kW/m^2$), thus imposing the overall stator losses which defines the rated current. A different value of the cooling system capacity would clearly lead to a different magnetic exploitation of the machine thus affect the consideration and the trade-off between overload torque and PM demagnetization during the short circuit. Fig. 12 reports the overload torque of the best designs with and without considering the demagnetization issue during a three phase short circuit, for three different k_{cool} scenario (i.e. $20kW/m^2$, $30kW/m^2$ and $40kW/m^2$). It
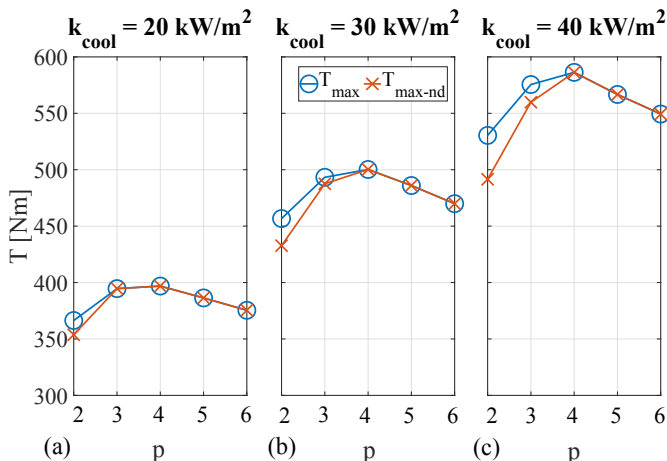
Fig. 12: Performance of the maximum torque designs as function of the number of poles and cooling extraction capability.

is worth noticing that lower k_{cool} implies a smaller difference between the solutions obtained with and without considering the PM demagnetization constraint. This is an expected result since higher cooling system capability also implies higher overload current which increases the ASC current and also reduces the pre-fault PM flux density. Going from low to high values of k_{cool}, so from low to high power density designs, the best torque-wise solution moves from 6 to 8 poles.

VI. EXPERIMENTAL RESULTS

The considerations reported in the previous sections lead to the conclusion that the design M4 represents the best compromise in terms of performance and robustness against demagnetization during the short circuit.

Therefore such machine has been selected as final candidate to be manufactured and tested. However, before commencing the prototyping an accurate design refinement has been performed so to take into account all the aspects disregarded during the analytical design approach, which mainly include the rotor structural and cooling system designs [29]. In particular, the orientation of the flux barriers as well as well the positioning and orientation of the iron ribs have been identified using structural FE analysis aimed at guaranteeing the rotor integrity up to 17 kprm keeping unchanged the analytically calculated PM volume. Regarding the thermal management, a combination of spray and shaft oil cooling has been selected as the best compromise between cost, structural simplicity, and cooling efficacy guaranteeing the safely extraction of the supposed stator total losses imposed with the k_{cool}. Fig. 13 reports the rotor stack (a), the assembled machine (b) and the final test rig layout (c) used for the torque measurement. The actual machine presents two set of three-phase windings which can be separately fed thus increasing the fault tolerance. The test bench setup includes an integrated inverter, the control platform and the motor under test (MUT) which is connected to the load motor throughout a gearbox. During the tests, no phase-shift between each three-phase set has been imposed, i.e. the machine has been treated as simple-three phase one.

In Fig. 14a an excellent match between the FE and experimental no-load line to line voltages at 2000 rpm can be observed. The comparison between MEC, FE and experimental torque is shown in Fig. 14b in terms of contour loci in the
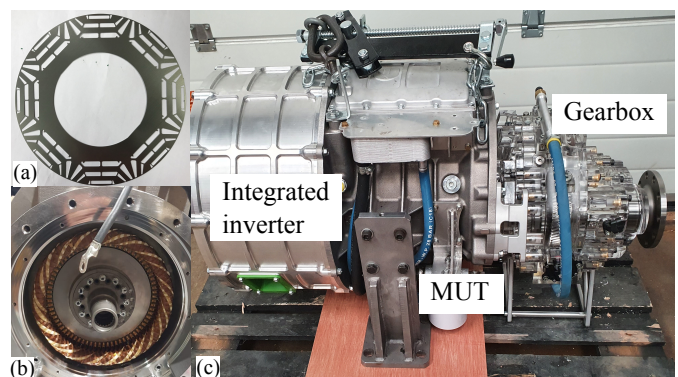
Fig. 13: (a) Final rotor lamination; (b) stator view; (c) assembled powertrain.

This article has been accepted for publication in IEEE Transactions on Energy Conversion. This is the author's version which has not been fully edited and content may change prior to final publication. Citation information: DOI 10.1109/TEC.2024.3508457

12
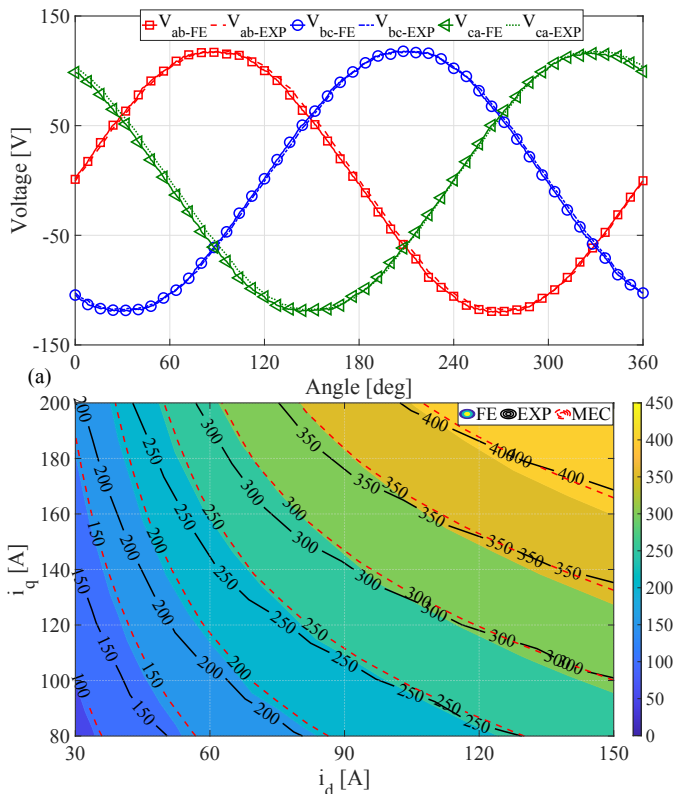
Fig. 14: (a) Comparison between FE and experimental line-to-line back electromotive forces; (b) comparison between MEC, FE and measured torque.

$i_d - i_q$. The MEC prediction perfectly matches the FE ones in the entire current plane while the experimental results shows a small discrepancy in the low current region.

VII. Conclusion

This paper has proposed a systematic design comparison for PMaSyRM for heavy-duty traction application, also considering the implications of the active short circuit technique in terms of PM demagnetization risk. First, a fully analytical performance evaluation method based on lumped-parameters MEC have been proposed, highlighting its accuracy in the prediction of the machine performance also in high saturation conditions and flux weakening region. Being computational inexpensive, the method has been embedded within a design procedure with the aim of inferring the trade-offs among the several performance indexes. In particular, the compromise between overload capability and PM demagnetizion risk during the symmetrical three phase short circuit has been investigated in the design plane split-iron ratio ($sr - ir$). The analysis, carried out for a given outer envelope and different pole pairs, leads to the following main findings.

- The designs featuring the maximum overload torque tends to move towards higher split ratio and lower iron ratio solutions as the number of pole increases. This is mainly due to the increasing effect of the iron losses.

- Designs featuring high ir and low sr may incur in the irreversible PM demagnetization during worst short circuit condition. This behavior is more pronounced for low pole pairs design.

- The PM demagnetization constraint during the worst short circuit condition affects the machine selection mainly when considering low pole designs.

References

[1] C. Liu, K. T. Chau, C. H. T. Lee, and Z. Song. A critical review of advanced electric machines and control strategies for electric vehicles. *Proceedings of the IEEE*, 109(6):1004–1028, 2021.

[2] R. Debouk. Overview of the second edition of iso 26262: Functional safety—road vehicles. *Journal of System Safety*, 55(1):13–21, 2019.

[3] S. Li, C. Chang, and H. Zhao. Functional safety development of e-motor drive system for phev. Technical report, SAE Technical Paper, 2015.

[4] S. Christiaens, J. Ogrzewalla, and S. Pischinger. Functional safety for hybrid and electric vehicles. sae paper no. 2012.

[5] R. R. Sabbella and M. Arunachalam. Functional safety development of motor control unit for electric vehicles. In *2019 IEEE Transportation Electrification Conference (ITEC-India)*, pages 1–6, 2019.

[6] A. R. Chandran, M. D. Hennen, A. Arkkio, and A. Belahcen. Safe turn-off strategy for electric drives in automotive applications. *IEEE Transactions on Transportation Electrification*, 8(1):9–22, 2022.

[7] K. Lu, Y. Zhu, Z. Wu, and M. Xiao. Suppression of current fluctuations and the brake torque for pmsm shutoff in electric vehicles. *Mathematical Problems in Engineering*, 2019(1):5026316, 2019.

[8] S. Chen, X. Hao, C. Gao, and Z. Jiang. An effective nontransient active short-circuit method for pmsm in electric vehicles. *IEEE Transactions on Industrial Electronics*, 70(4):3571–3580, 2023.

[9] P. Ragazzo, G. Dilevrano, S. Ferrari, and G. Pellegrino. Comparative turn-off safe modes of ferrite- and ndfeb- interior pmsms. In *2023 IEEE Energy Conversion Congress and Exposition (ECCE)*, pages 4133–4139, 2023.

[10] J. Choi and Y. Kim. Discontinuous active short circuit strategy for improved safe state of pmsms. *IEEE Transactions on Transportation Electrification*, pages 1–1, 2024.

[11] T.M. Jahns and V. Caliskan. Uncontrolled generator operation of interior pm synchronous machines following high-speed inverter shutdown. *IEEE Transactions on Industry Applications*, 35(6):1347–1357, 1999.

[12] G. Pellegrino, A. Vagati, and P. Guglielmi. Design tradeoffs between constant power speed range, uncontrolled generator operation, and rated current of ipm motor drives. *IEEE Transactions on Industry Applications*, 47(5):1995–2003, 2011.

[13] B. A. Welchko, T. M. Jahns, and J. M. Soong, W. L.and Nagashima. Ipm synchronous machine drive response to symmetrical and asymmetrical short circuit faults. *IEEE Transactions on energy conversion*, 18(2):291–298, 2003.

[14] G. Choi and T. M. Jahns. Investigation of key factors influencing the response of permanent magnet synchronous machines to three-phase symmetrical short-circuit faults. *IEEE transactions on energy conversion*, 31(4):1488–1497, 2016.

[15] S. Ferrari, G. Dilevrano, P. Ragazzo, P. Pescetto, and G. Pellegrino. Fast determination of transient short-circuit current of pm synchronous machines via magnetostatic flux maps. *IEEE Transactions on Industry Applications*, 59(4):4000–4009, 2023.

[16] Hanafy Mahmoud, Nicola Bianchi, Giacomo Bacco, and Nicola Chiodetto. Nonlinear analytical computation of the magnetic field in reluctance synchronous machines. *IEEE Transactions on Industry Applications*, 53(6):5373–5382, 2017.

[17] S-H Han, T. M. Jahns, and W. L. Soong. A magnetic circuit model for an ipm synchronous machine incorporating moving airgap and cross-coupled saturation effects. In *2007 IEEE International Electric Machines & Drives Conference*, volume 1, pages 21–26, 2007.

[18] G. Gallicchio, M. Di Nardo, F. Cupertino, V. Varvolik, G. Buticchi, M. Degano, and C. Gerada. Fast flux maps computation of synchronous reluctance machines with and without permanent magnets assistance. *IEEE Transactions on Industry Applications*, 60(5):6725–6735, 2024.

[19] A. M. Silva, C. H. Antunes, A. M. S. Mendes, and F. J. T. E. Ferreira. Generalized reluctance network framework for fast electromagnetic analysis of radial-flux machines. *IEEE Transactions on Energy Conversion*, pages 1–11, 2022.

[20] L. Ding, G. Liu, Q. Chen, and G. Xu. A novel mesh-based equivalent magnetic network for performance analysis and optimal design of permanent magnet machines. *IEEE Transactions on Energy Conversion*, 34(3):1337–1346, 2019.

[21] A. Hemeida, A. Lehikoinen, P. Rasilo, H. Vansompel, A. Belahcen, A. Arkkio, and P. Sergeant. A simple and efficient quasi-3d magnetic equivalent circuit for surface axial flux permanent magnet synchronous machines. *IEEE Transactions on Industrial Electronics*, 66(11):8318–8333, 2019.

[22] A. Vagati, G. Franceschini, I. Marongiu, and G. P. Troglia. Design criteria of high performance synchronous reluctance motors. In *Industry Applications Society Annual Meeting, 1992., Conference Record of the 1992 IEEE*, pages 66–73 vol.1.

[23] S. Ferrari and G. Pellegrino. Feafix: Fea refinement of design equations for synchronous reluctance machines. *IEEE Transactions on Industry Applications*, 56(1):256–266, 2020.

[24] M. Di Nardo, G. Gallicchio, M. Palmieri, A. Marfoli, G. Lo Calzo, M. Degano, C. Gerada, and F. Cupertino. High-speed synchronous reluctance machines: Materials selection and performance boundaries. *IEEE Transactions on Transportation Electrification*, 8(1):1228–1241, 2022.

[25] C. Babetto, G. Bacco, and N. Bianchi. Analytical power limits curves of high-speed synchronous reluctance machines. *IEEE Transactions on Industry Applications*, 55(2):1342–1350, 2019.

[26] A. Vagati, B. Boazzo, P. Guglielmi, and G. Pellegrino. Design of ferrite-assisted synchronous reluctance machines robust toward demagnetization. *IEEE Transactions on Industry Applications*, 50(3):1768–1779, 2014.

[27] M. Di Nardo, G. Gallicchio, F. Cupertino, O. Korman, M. Wang, C. Gerada, V. Varvolik, S. Wang, and G. Buticchi. Permanent magnet assisted synchronous reluctance machine design for light traction applications. *IEEE Transactions on Industry Applications*, pages 1–14, 2024.

[28] G. F. Olson, S. Ferrari, A. Bojoi, P. Pescetto, L. Peretti, and G. Pellegrino. Guaranteed torque and demagnetization current during active short-circuit transients of pmsms. In *2024 IEEE International Conference on Industrial Technology (ICIT)*, pages 1–8, 2024.

[29] T. Zou, D. Gerada, S. La Rocca, A. La Rocca, A. Walker, G. Vakil, S. L. Arevalo, Z. Xu, M. Cui, A. Bardalai, M. Wang, R. M. R. Kumar, A. Marfoli, K. Paciura, R. Barden, E. Ernest, S. Zhu, N. Qayyum, A. McQueen, F. Zhang, and C. Gerada. Airgap length analysis of a 350 kw pm-assisted syn-rel machine for heavy duty ev traction. *IEEE Transactions on Industry Applications*, 59(2):1557–1570, 2023.